Science and Technology Indonesia
e-ISSN:2580-4391 *p*-ISSN:2580-4405
Vol. 10, No. 2, April 2025

Research Paper

Clitoria ternatea Flower Extract Mediated Synthesis of Ni-Doped Hydroxyapatite as Photocatalyst, Antibacterial, and Drug Delivery Agent for Anticancer Drug

Is Fatimah[1,2*], Nunung Nurlaela[1,2], Anas Zahra Fauziyyah[1,2], Suresh Sagadevan[3], Habibi Hidayat[1], Mehru Nisha Muhamad Haneef[4], Muhammad Fauzi Daud[4], Azlan Kamari[5], Won-Chun Oh[6]

[1]*Department of Chemistry, Faculty of Mathematics and Natural Sciences, Universitas Islam Indonesia, Yogyakarta, 55584, Indonesia*
[2]*Nanomaterials and Sustainable Chemistry Research Centre, Universitas Islam Indonesia, Chemistry Research Building, Kampus Terpadu UII, Yogyakarta, 55584, Indonesia*
[3]*Nanotechnology & Catalysis Research Centre, University of Malaya, Kuala Lumpur, 50603, Malaysia*
[4]*Institute of Medical Science Technology, Universiti Kuala Lumpur (UniKL), Selangor, 43000, Malaysia*
[5]*Chemistry Department, Faculty of Science and Technology, Universiti Pendidikan Sultan Idris, Perak, 35900, Malaysia*
[6]*Department of Advanced Materials Science and Engineering, Hanseo University, Seosan-Si, 356-706, South Korea*
***Corresponding author**: isfatimah@uii.ac.id

Abstract
In the present study, green synthesis of nickel-doped hydroxyapatite using *Clitoria ternatea* flower extract, and activity testing as photocatalyst, antibacterial agent and drug delivery agent were performed. Synthesis was conducted by hydrothermal treatment of co-precipitated precursors previously mediated with the extract. As drug delivery agent, immobilization of 5-fluorouracil (5FU) onto the prepared sample was performed by spray-drying method. Physicochemical characterization techniques of X-ray diffraction, UV-Visible Diffuse Reflectance Spectrophotometry, transmission electron microscopy, Raman and Fourier-Transform Infra-red spectroscopy were performed to determine the structural and surface properties of material. Photocatalytic activity evaluation for tetracycline removal showed that material has capability to reduce concentration by photocatalytic degradation and photocatalytic oxidation. The degradation efficiency of material was 83.78%. The prepared material exhibited a significant activity against *Staphylococcus aureus* and *Escherichia coli* bacteria. The material also expressed the potency as a drug-delivery agent of 5-fluorouracil as shown by the reduced CT26 cell viability of more than 85% during 48 hours.

Keywords
Antibacterial Agent, Drug Delivery System, Hydroxyapatite, Nickel-Doped Hydroxyapatite, Photocatalyst

Received: 15 October 2024, Accepted: 21 January 2025
https://doi.org/10.26554/sti.2025.10.2.360-373

1. INTRODUCTION

As the impact of industrialization and abundant chemical products for daily life, environmental pollution and healthcare are the important concerns recently. Pharmaceuticals and healthcare industries are highly water consuming sectors. In other side, the effect of organic-contaminated water and soil are becoming a terrible issue, including the increasing cancer diseases (Berkün Olgun et al., 2021; Chen et al., 2022). Environmental problems caused by pharmaceuticals pollutant, bacterial infection, and cancer treatment require an emerging technology for recovery. Advanced oxidation process (AOPs) by the light exposure in a photocatalytic system is a well-known method of water remediation (Shaheen et al., 2022).

Hydroxyapatite (HA) and its modified form have been recognized as important materials for environmental and biomedical applications. The chemical composition, porosity and modifiable surface structure of HA are potential to provide surface active site, so it could be effective as metal or metal support as well as the host for some organic compounds for being active for various purposes, including photocatalysis (Fihri et al., 2017; Mondal et al., 2023). The doping of HA with some metals is one of functionalization strategies to improve the performance and effectiveness of nanocomposite for some important reactions. Regarding to the capability to be host for drug compounds, HA and metal-modified form could be arranged as the advanced and innovative drug delivery systems. Various metal-doped HA such as Ag/HA, Au/HA, Zr/HA and Ti/HA have been reported to be efficient in facilitating the acceleration photoactivity, catalytic activity, and many other purposes for air and water pollution, drug-delivery, and bacterial disinfection (Fatimah et al., 2021a, 2020; Robles-Águila et al., 2017).

This functionalization is potential and inspires future ad-

vancements in medical technology. Since the development of HA and related minerals achieved a successful role in various bone and tissue engineering, its role as drug carrier for some antibacterial, antifungal, antibiotics, and anticancer is now demanding (Varadavenkatesan et al., 2021; Yadav et al., 2023). Considering the great challenges for the advancement of cancer drugs, in this study, the potential of HA and Ni-doped HA as cancer drug carrier agents was studied.

Advancements in searching for efficient and economic synthesis method of functionalized HA tend to the use of green chemistry approach. Besides using some intensification procedures such as microwave-assisted irradiation or ultrasound-assisted synthesis, the metal dopant nanoparticles could be produced by utilizing plant extracts as bio-reductors. Previous investigations revealed that the use of plant extracts is a suitable option as the benign process of the synthesis of silver, gold, nickel, tin oxide, and iron oxide nanoparticles (Al-darwesh et al., 2024; Azizi, 2020; Mohammad et al., 2021; Naveenkumar and Baskar, 2021). The incorporation of green synthesized metal nanoparticles into HA structure demonstrated the enhanced antibacterial and antioxidative activity of the nanocomposite with comparable performance respect to the general method synthesized metals. Plant extracts with high containing secondary metabolites such as alkaloid, flavonoids, and polyphenols have the capability to reduce metal precursors, and in addition, form stable complexes as capping agent to nanoparticles. Among some plants, *Clitoria ternatea* is kind of plant which well-known as rich plant in secondary metabolites as it is generally utilized in healthy and functionalized food and beverages components. *Clitoria ternatea* extract (CTE) has been proven to be effective in the synthesis of Ag, Au, Sn, and Fe nanoparticles (Fatimah et al., 2021b, 2020; Khwannimit et al., 2020; Poh Yan et al., 2022). Based on these backgrounds, in this research, CTE was used as bio-reductor in synthesis of nickel nanoparticles (NiNPs) was dopant of HA. The NiNPs were then used for functionalization of HA. The use of CTE-synthesized metal nanoparticles as dopant of HA and the applicability of nanocomposite as photocatalyst, antibacterial agent, and anticancer drug-delivery are the novelty of this research. Considering the important concern on colon cancer treatment, 5-fluorouracil (5FU) was selected to be a drug model anchored onto HA and Ni/HA samples, and the testing was performed for CT26 cell line as representation of colon cancer. Previous studies showed the functionalization of some drug delivery agent with 5FU is potential to increase antitumor efficacy and improve patient survival. To authors knowledge, this topic is never reported yet. Study on the synthesis method on physicochemical characteristics, antibacterial and capabilities of the nanomaterial as cancer-drug delivery agent was aimed at this study.

2. EXPERIMENTAL SECTION

2.1 Preparation of CTE

About 4 g of the fresh *Clitoria ternatea* flowers were obtained from the community plantation area in Sleman District, Yogyakarta Special Province, Indonesia. The flowers were crushed on mortar and followed by the addition of demineralized water with water, stirring, and separation from debris using Whatman 41 filter paper. The obtained filtration was denoted as CTE.

2.2 Chemicals

The chemicals used are nickel chloride dihydrate ($NiCl_2.2H_2O$, Sigma Aldrich, purity > 95%), calcium oxide (CaO, Merck, purity > 95%), ammonium dihydrogen phosphate $(NH_4)_2HPO_4$, Sigma Aldrich, purity > 95%), sodium hydroxide (NaOH, Sigma Aldrich, purity > 95%), tetracycline (Sigma Aldrich, purity > 95%), and 5-fluorouracil (5-FU)(Sigma Aldrich, purity > 95%).

2.3 CTE-Mediated Synthesis of Ni/HA (Ni(CT)/HA)

The green synthesis procedure of Ni(CT)/HA by using CTE was carried out by hydrothermal coprecipitation method. The procedure consist of 2 (two) steps; synthesis of NiNPs, and utilization of the obtained NiNPs to produce Ni(CT)/HA. NiNPs obtained by mixing CTE with Ni^{2+} solution under the condition of Ni concentration of 0.01 M, and CTE to Ni volume of 1:1, followed by reflux for 40 °C. Separatedly, an aaqueous solution of calcium oxide and ammonium dihydrogen phosphate were mixed under the condition of (Ca+Ni)/ P molar ratio of 1.67 as a Ca/P stoichiometric ratio of Hap structure. The concentration of Ca was taken ranging at 0.025-0.2 mol L^{-1}. The mixed solutions were poured into a-Teflon-lined autoclave and kept at 150 °C overnight. A slurry derived by these steps were then washed using demineralized water until the filtrate was Cl^- free.

As comparison, the synthesis of Ni/HA was performed by using $NiCl_2.2H_2O$ as precursor instead of NiNPs. Similarly, the HA was also prepared without Ni addition as precursor (furthermore called as HA), and synthesis using Ni^{2+} solution.

2.4 Immobilization of 5FU onto HA and Ni/HA

The attachment of 5FU onto HA and Ni/HA samples was carried out by previous research on functionalization of HA using 5-FU (Scharnweber et al., 2008). The method presented by mixing 5-FU solution with the HA, Ni/HA and Ni(CT)/HA powders followed by stirring for 3h. The obtained mixture was then freeze-dried to get powder of 5-FU/HA, 5-FU-Ni/HA and 5-FU-Ni(CT)/HA, respectively.

2.5 Physical Characterization of Prepared Materials

The synthesized HA and Ni/HA samples were analyzed by structural, optical, and surface studies. Structural characterization determined using an X-ray diffractometer on XRD PANalytical operated using Ni-filtered Cu- Kα radiation (k= 1.54 Å) at the 2θ ranging at 10-70°. The optical properties were observed on UV-DRS spectrophotometer (Shimadzu 2700) with $BaSO_4$ as standard. A Fourier-Transformed infrared spectroscopy (FTIR Perkin-Elmer) and Raman spectrometer (HORIBA) were employed to investigate the presence of functional groups evolution, meanwhile a HORIBA particle

size distribution and zeta analyzer were employed to determine the particle's distribution and electronic state of the surface. JEOL-JEM-2010 (Japan) Transmission Electron Microscopy was employed to identify detail of particle form and size. Surface analysis of X-ray photoelectron spectroscopy (XPS) was conducted using a ULVAC XPS instrument (Quentera SXM, Japan).

2.6 Photocatalytic Oxidation of TC

The photocatalytic activity of Ni/HA was examined to reduce TC in a batch photoreactor. For each experiment, 0.2 g of Ni/HA powder was dispersed into a 250 mL of 5 mg/L TC solution, and then was stirred under light (UV and Visible light) exposure. To determine the concentration of treated solution, colorimetric analysis on UV-Visible spectrophotometry was performed. The samples were sequentially collected at certain time to furthermore the data was processed to evaluate the kinetics and determine the degradation efficiency (DE). The DE is referred to following Equation (1):

$$DE(\%) = \frac{TC_i - TC_f}{TC_i} \times 100\% \quad (1)$$

Where TC_i and TC_f are initial concentration and concentration at sampling time of t.

2.7 Antibacterial Assay

Bacterial strains of gram-negative *Escherichia coli* and gram-positive *Staphylococcus aureus* were employed to examine the antibacterial activity of prepared samples. The applied method was the agar well diffusion. Broth medium was first sub-cultured and incubated at 37 °C for 24 h, followed by an overnight culture on the agar plates to cultivate a uniform microbial growth. For the assay, the samples powder at the concentration of 5 mg/5 mL was dispersed in demineralized water, followed by loading onto a 6 mm filter disc. The obtained discs were placed on bacterial culture in the Petri plate for a 24 h incubation. Measurement of clear zone was taken as the inhibition zone of each sample.

2.8 Cytotoxicity Assessment of 5FU-Ni/HA Colon Cell Line (CT26)

For cytotoxicity assessment of 5FU-Ni/HA, the CT26 colon cancer cells were seeded in a 96-well plate and cultured overnight. Into the culture media, the 5FU-Ni/HA dispersion in water (concentration of 5 mg/100 mL) was added, followed by 48 h of incubation. The cytotoxicity of the 5FU-Ni/HA was calculated as follows (Equation (2)):

$$\text{Viability}\ (\%) = \left(\frac{\text{Mean absorbance of sample}}{\text{Mean absorbance of control}} \times 100\right) \quad (2)$$

Figure 1 provide a schematic procedure of synthesis, characterization and activity test of Ni(CT)/HA in this research.

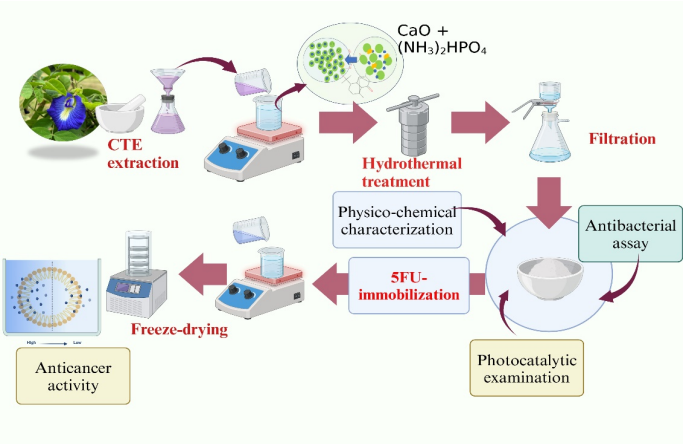

Figure 1. Schematic Procedure of This Research.

3. RESULTS AND DISCUSSION

Initial evaluation of NiNPs formation was conducted using UV-Visible spectrophotometric analysis method. By optimizing Ni^{2+}: CTE volume ratios, it was obtained that 0.01 M Ni^{2+}: CTE of 1:1 ratio formed the NiNPs as identified by UV-Visible spectra provided in Figure 2.

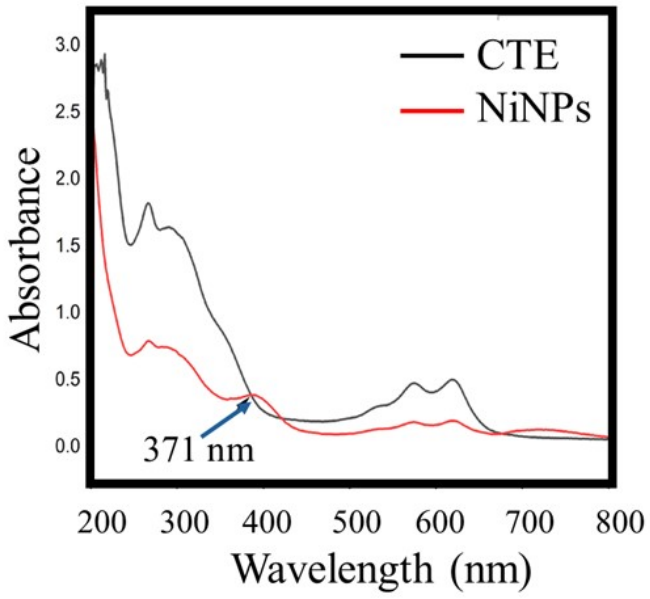

Figure 2. UV-Visible Spectra of CTE and NiNPs

The UV-Visible spectrum of CTE shows peaks at around 230 nm, 570 nm, and 620 nm as identifications for the presence of aromatic structures from secondary metabolites of anthocyanin (Prabhu et al., 2022). After being used to reduce Ni^{2+}, the peaks are reduced implying the reactions to anthocyanin. In addition, there is an additional peak at 371 nm which is indication of the formation of surface plasmon resonance related to the formation of NiNPs (Balto et al., 2023;

Yeshchenko et al., 2018). Based on some previous literature, CTE consists of some compounds such as fibre, protein, carbohydrate, vitamin and some secondary metabolites. Previous analysis by high performance liquid chromatography revealed that anthocyanins known as ternatins which have blue color and are acylated based on delphinidin were the dominant compounds. 3-hydroxy-3',4'-dimethoxyflavone is one of the compounds (Jiji and Muralidharan, 2021; Jeyaraj et al., 2021). As the secondary metabolites have sufficient structures as the bio-reductor, the Ni^{2+} could be reduced into Ni^{0} surrounded with the compounds as capping agent. Taking into account that 3-hydroxy-3',4'-dimethoxyflavone exists in the CTE, the reduction mechanism could be schematically represented as depicted in Figure 3.

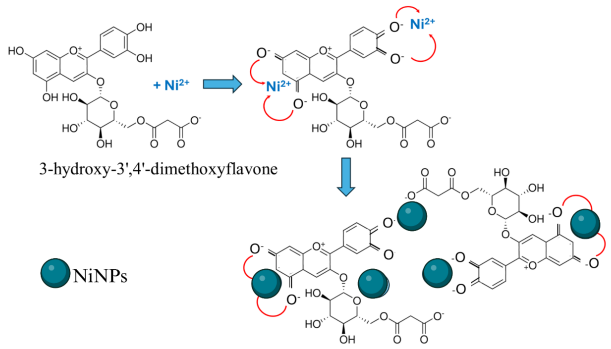

Figure 3. Mechanism of Bio-Reduction by 3-Hydroxy-3',4'-Dimethoxyflavone in CTE [Adapted from Yoga Darmawan et al. (2023)

3.1 XRD Analysis

The results from XRD analysis are provided in Figure 4. The reflection peaks of HA sample fit with the standard pattern of HA which shows the (102), (210), (211), (112), (300), (130), (222), (132), and (213) referred to JCPDS File No: 9-0432.

There is no other peak identifying CaO or phosphate minerals suggesting neither excess reactants nor other calcium phosphate as the byproducts of the synthesis. After dopped with Ni, some other peaks at 23.06°, 23.16°, 28.07°, 34.74°, 36.07°, 47.64°, and 56.62° appeared by both Ni/HA and Ni (CT)/HA. Those peaks are identification for the formation of β-tricalcium phosphate (β-TCP), referred to the JCPDS File No. 09-0169. The occurring β-TCP is related to the presence of Ni metal which affects to the crystal formation and Ca/P molar ratio during coprecipitation and sintering mechanism. This process is described by thermal transformation of precipitated HA into β-TCP at around 800 °C for 5 h by previous investigation (Mayer et al., 2008). With a certain condition influencing Ca/P ratio and co-precipitation mechanism, the HA partially decomposes and transforms into β-TCP according to the following reaction:

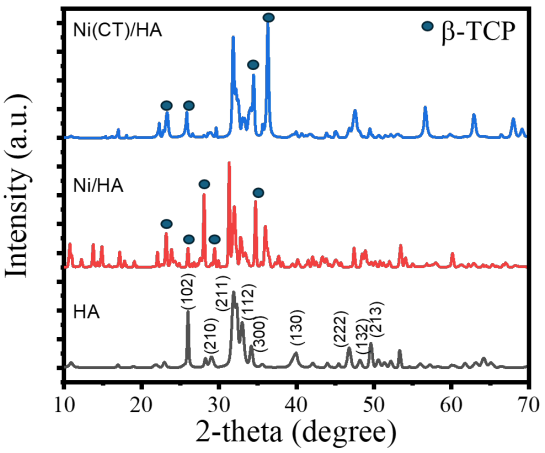

Figure 4. XRD Patterns of Prepared Materials

$$Ca_{10}(PO_4)_6(OH)_2 \rightarrow 2Ca_3(PO_4)_2 + Ca_4(PO_4)_2O + H_2O$$

The phenomenon was similar to previous investigations on HA doping by Zn (Mardziah et al., 2023), Fe (Anastasiou et al., 2016), and Mg (Kanchana and Sekar, 2012).

Using important peaks of HA, the crystalline size of the materials was calculated using Scherer's equation defined elsewhere (Abdel-Aal et al., 2024), and detail of calculation is as depicted in Table 1.

From the calculated data, it is obtained that doping increases the crystallite size of HA. This is an inverse phenomenon compared to some studies reported on the effect of metal dopant to the HA structure. Previous research on Ni doping to HA gave a reduced crystallite size, similarly, the doping by using Mg, Li, Zn, and Ni (Kanasan et al., 2018; Nicácio et al., 2024; Kurinjinathan et al., 2020; Wang et al., 2016). The reduced crystallite size and crystallinity is due to the inclusion of carbonates in the HA structure which correlated to the change of lattice parameters. In general, crystallite size depends on many factors, including temperature of crystallization. Hydrothermal conditions and pH participates to lead the increased crystallization (Abdel-Aal et al., 2024; Liang et al., 2012; Silva et al., 2007). As the phase transition of HA to β-TCA is facilitated by the hydrothermal condition, the increased crystallization should be related to the reaction condition. As can be seen that Ni(CT)/HA has highest crystallite size, it means that the compounds containing in the CTE influence the coprecipitation mechanism. The possible interaction between functional groups with Ca^{2+} and PO_4^{3-} affects to the crystal growth of HA (In et al., 2020).

Table 1. Calculation of Materials Crystallite Size Based on XRD Data

Peak Position	HA		Ni/HA		Ni(CT)/HA	
	FWHM	Crystalline Size (nm)	FWHM	Crystalline Size (nm)	FWHM	Crystalline Size (nm)
26.03	0.199	42.70	0.190	44.80	0.191	44.3
31.89	0.547	15.70	0.376	22.95	0.254	34.00
32.98	0.756	22.20	0.520	16.70	0.312	27.7
34.17	0.373	24.70	0.340	32.80	0.26	32.80
	Crystallite size mean = 24.45 nm		Crystallite size mean = 29.31 nm		Crystallite size mean = 34.70 nm	

3.2 TEM Analysis

TEM analysis was employed to evaluate the morphology and particle's size distribution of prepared material. Figure 5 shows that Ni(CT)/HA express a smaller particle size compared to Ni/HA, which by the particle size distribution, the means particle size of Ni(CT)/HA, Ni/HA and HA are 23 nm, 119 nm, and 1900 nm, respectively. Due to morphologies, Ni(CT)/HA shows slightly different and heterogeneous form compared to Ni/HA which exhibits a rod-like form. Similarly, the HA has rod-like with longer size. The evolution of morphology is correlated to the structural transformation of HA into TCP. In addition, the smaller particle size represents the role of CTE as the templating and chelating agent during co-precipitation and crystallization of HA structure. The assumption is referred to previous similar works in utilizing plant extract for HA and metal-doped HA syntheses (Alorku et al., 2020).

Flavonoids and some tannic acids from Moringa olifiera flower extract was act as chelating agent to govern the co-precipitation which responsible to the particle's size distribution (Sundrarajan et al., 2015). Similar mechanism was proporsed by utilizing *Marrubium astracanicum* in the synthesis of Ag/hydroxyapatite (Unal et al., 2024).

3.3 FTIR and Raman Analysis

Raman analysis to Ni(CT)/HA sample (Figure 6a) identifies the presence of phosphate ions in the HA structure. The peaks characteristic of HA structure is exhibited at 449, 590, and 968 cm^{-1} that are associated with the doubly degenerate bending mode $v2(PO_4^{3-})$, triply degenerate bending mode $v3(PO_4^{3-})$ and totally symmetric stretching mode $v1(PO_4^{3-})$, respectively. The peaks are shifted from the characteristic peaks in HA at 427, 589 and 960 cm^{-1}, respectively (Prekajski et al., 2016; Yuan et al., 2017). This implies that the band of PO_4^{3-} is changed with the incorporated Ni which corresponds to a distorted PO_4^{3-} structure. This data is in line with the XRD result corresponding to the identified structural transformations of HA into β-TCA by Ni-doping.

FTIR analysis was employed to study the change of functional groups in the materials. Figure 6b illustrates the spectra. HA demonstrates the phosphate group, PO_4^{3-} characteristic observed at 561.9 and 601 cm^{-1}. Those bands are also correlated to the absorption at 1059 cm^{-1}. In addition, the band at 1581 cm^{-1} is attributed to the presence of the hydroxyl groups. For all samples, the bands at around 2918 and 2848 cm^{-1} are found, that are correlated to the CO_2 adsorbed by the samples during the analysis. After the insertion of Ni into HA structure (Ni(CT)/HA, those bands showed the shifting into higher wavenumbers. The band at 561 cm^{-1} is shifted into 563 cm^{-1}, and in same way, the band at 1059 cm^{-1} is shifted into 1060 cm^{-1}, and from 1581 cm^{-1} into 1589 cm^{-1}.The increased wavenumber implies the higher bonding energy caused by the interaction of Ni^- with O−H or O−P−O bonds in the structure, leading to the higher bending or stretching energies. After modified with 5FU, some additional peaks at around 1458 cm^{-1} and 1410 cm^{-1} are the indication of aromatic ring from pyridinium, and the band at 961 cm^{-1} represents the CH_3- from 5FU. Schematic figure of 5FU attachment onto HA surface is presented in Figure 7. Beside of the insertion of 5FU molecules into the pore sites of HA, coordination bonding are possible from the availability of Ca^{2+} , H and O^- in the HA with F, and O having electron pairs, and H.

3.4 Optical Property of Ni/HA

Band gap energy is a physical property which correlated to photocatalytic activity of the nanomaterial. UV-DRS spectrum of the Ni(CT)/HA sample in comparison with Ni/HA sample is depicted in Figure 8. As can be seen from the spectra, the extrapolations of the plots gives the band gap energy values for Ni(CT)/HA and Ni/HA are 2.95 eV and 2.90 eV, respectively. The values indicate the capability of nanomaterials to catch photons within the visible range. The values are notified as higher than were reported by previous work comparable to the similar material of Ni-doped hydroxyapatite which showed the band gap of 2.1 eV (Mohammed et al., 2018) The band gap energy of composite is related to the contributing band gap energy of nickel nanoparticles and HA (Fatimah et al., 2023, 2024).

Photocatalytic activity evaluation Photocatalytic activity of prepared Ni(CT)/HA was examined in TC removal via photocatalytic degradation (photodegradation) and photocatalytic oxidation (photooxidation) under varied light source; UV light and visible light. In principle, the reaction was performed by mixing the nanocomposite with TC solution in a batch photocatalytic reactor equipped with UV and Visible (xenon) lamp as photon source. The difference between both treatments is on the use of H_2O_2 in photooxidation. The kinetics plots of TC removal over Ni(CT)/HA are provided in Figure 9a. The plots imply that photooxidation gave faster TC removal compared to

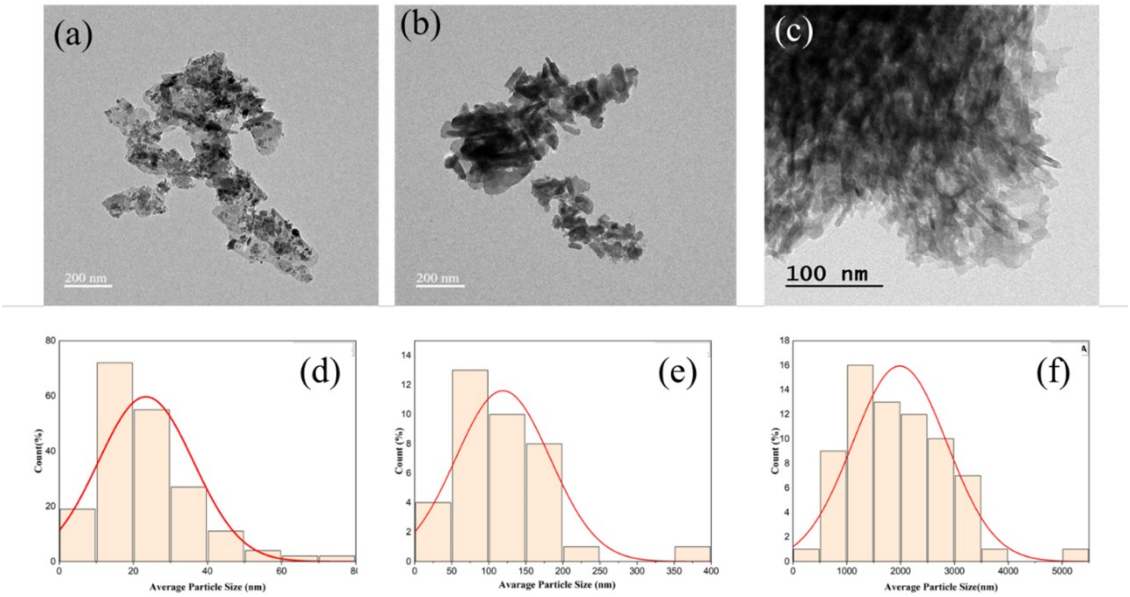

Figure 5. (a-c) SEM Images, (d-f) Particle's Size Distribution of Ni(CT)/HA, Ni/HA, and HA, Respectively

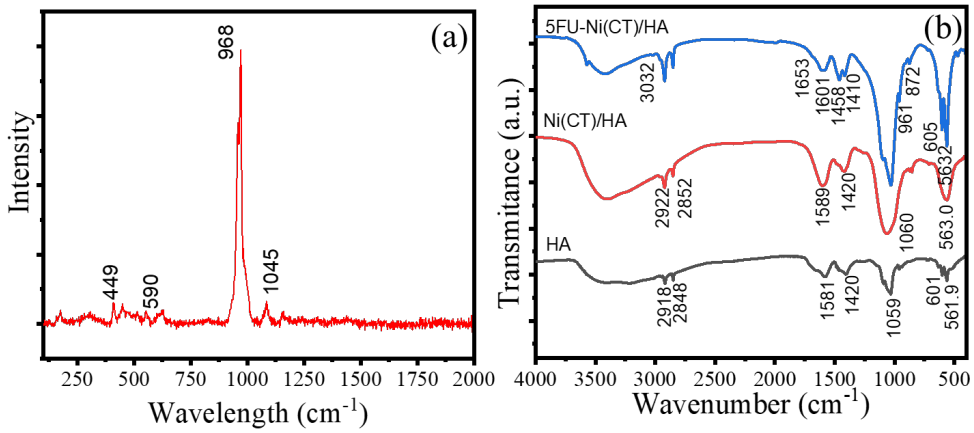

Figure 6. a. Raman Spectrum of Ni(CT)/HA, b. FTIR Spectra of Prepared Materials

photodegradation. By different light sources, UV accelerate the reaction faster than Visible light. By applying kinetics equation of pseudo-first-order and pseudo second-order kinetics with following equations (Equations 3-4):

$$ln\frac{C_t}{C_0} = -k_1 t \quad (3)$$

$$\frac{1}{C_t} = k_2 t + 1\frac{1}{C_0} \quad (4)$$

With C_0 and C_t are the initial TC concentration and concentration at the time of t, k_1 and k_2 are the first-order and pseudo-second order kinetics constants, respectively.

Conclusively, the photooxidation obeys pseudo second-order kinetics, while photodegradation fit to the pseudo first-order kinetics. The second-order kinetics plot of TC photooxidation by using Ni(CT)/HA and Ni/HA is represented in Figure 9b. This suggests that the addition of H_2O_2 signifies the oxidation mechanism.

As the nanocomposite impinged by the photon with sufficient or higher energy respect to the band gap energy, the electron in valence band will be excited into valence band. The excitation leads to the h+ in the valence band. The interaction of h+ with solvent or available oxidant in the system produces HO•, which furthermore could activated to produce more radicals including super radicals (•OOH). In other side, surface interaction between electron and H^+ from the solvent of reactant or available protonic species from organic compound release HO• (Far et al., 2022; Haider et al., 2019). The more

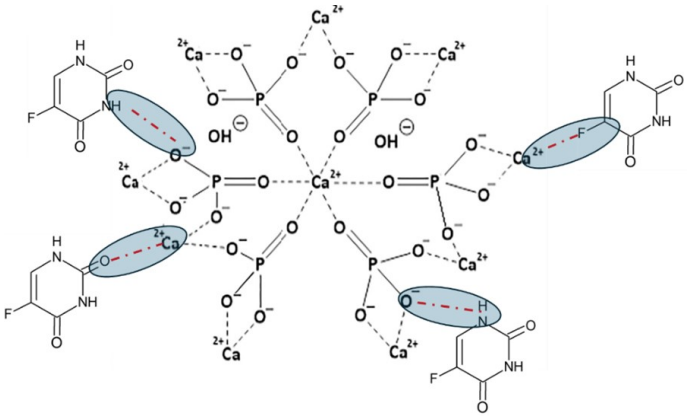

Figure 7. Scheme of Possible Interactions between HA and 5FU

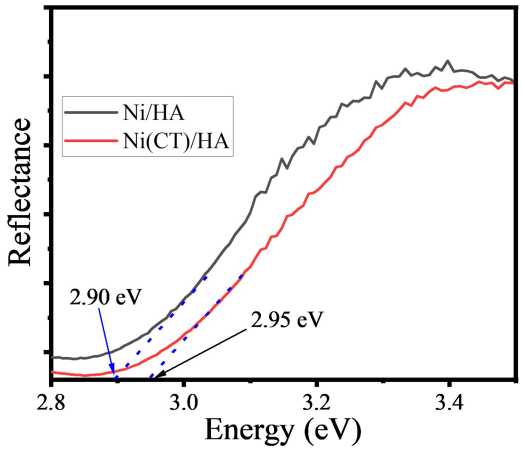

Figure 8. UV-DRS Spectra of Ni(CT)/HA and Ni/HA

HO• and •OOH formed at the initiation step, the higher potency of oxidants produced by propagation steps, referred to following mechanism:

$$\begin{aligned}
\text{Ni/HA} + h\nu &\rightarrow \text{Ni/HA-h}^+ + e^- \\
\text{Ni/HA-t}^+ + \text{OH}^- &\rightarrow \text{HO} + O_2 \\
\text{Ni/HA} + \text{H}_2\text{O}_2 &\rightarrow \text{Ni}^{2+} - \text{HA} + \text{OH}^+ + \text{HO} + O_2 + e^- \\
2\text{HO} + O_2 &\rightarrow 2\text{OOH} \\
O_2 + e^- &\rightarrow O_2^{2-} \\
O_2 + 2H^+ + 2e^- &\rightarrow \text{H}_2\text{O}_2 \\
\text{H}_2\text{O}_2 + e^- &\rightarrow \text{OH} + \text{OH}^- \\
\text{TC} + \text{HO} + O_2 &\rightarrow \text{Degradation products} \\
&\rightarrow \text{CO}_2 + \text{H}_2\text{O}
\end{aligned}$$

The occurrence of oxidation or degradation instead of adsorption is confirmed by the spectral change of solution after photodegradation and photooxidation in Figure 9c and 9d, respectively. There are not only reduced absorbance value of the treated solutions, but the shifting of maxima wavelength of TC (380 nm) into the right side are identified. These redshifts indicate the degradation of TC structure.

The more active Ni(CT)/HA than Ni/HA is proven by calculated parameters of kinetics constant (k) of each process listed in Table 2. The higher DE and k of photodegradation using UV light suggest the role of band gap energy for enhancing the capability to produce more stable radicals. The higher DE compared to the use of visible light is associated with the higher energy for releasing radicals. The higher band gap energy facilitates the excitation of electron into conductance band to be more stable cause of the inhibited recombination. It provides longer time to produce radicals and super radicals. Moreover, as the system rich in oxidant, the production of radicals will be more intensive, so the photooxidation gave the higher DE. In addition, the participation of H_2O_2 in the kinetics is represented by the 2nd order kinetics, meanwhile photodegradation obeys first-order kinetics.

3.5 Antibacterial Assay

Antibacterial activity of Ni(CT)/HA was examined against *S. aureus* and *E. coli*, by measuring the inhibition diameters of bacterial cultivation. The size of the clear zone surrounding every bacterial colony reflects that the area is affected by active site of the nanomaterials. Figure 10 presents some images and recapitulated data of the inhibitory diameter rate (in mm) for each of the infectious bacteria.

The results showed that Ni/HA and Ni(CT)/HA inhibited bacterial growth in a higher level respect to HA. These data are related to the presence and effectiveness of Ni in the Ni/HA structure as an active site which could release Ni^{2+} ions into cell environment. Ni^+ and Ca^{2+} ions interact to the cellular wall of gram-positive and gram-negative bacteria by adhesion and electrostatic forces. An ionic interaction between Ni^{2+} ions and some negative charges at the bacterial cell walls leads to cell lysis (Ilbeigi et al., 2019; Yilmaz et al., 2023). In case of gram-negative bacteria, *E. coli*, the envelope is composed by two lipid membranes with high concentrations of lipopolysaccharides, lipoprotein and porin channels in the outer leaflet of the outer membrane. Gram-negative bacterial have a thinner peptidoglycan layer compared to gram-positive, and in same time, gram-positive cell wall contains teichoic acids and lipoteichoic acids which contribute to the wall's rigidity. The condition causes the activity against *E. coli* is higher than to *S. aureus*.

The antibacterial activity of obtained samples are comparable to that were gained by some metal-doped hydroxyapatite such as Au-doped HA (Fatimah et al., 2021a), Ag-doped HA (Fatimah et al., 2022; Silva et al., 2007), and Ti-doped HA (Fatimah et al., 2023). Table 3 provides a comparison of antibacterial activity with some metal-doped hydroxyapatites.

The nanoparticles and electronic charges on Ni/HA surface led to ion extrusion through cell membrane. The ions inhibit

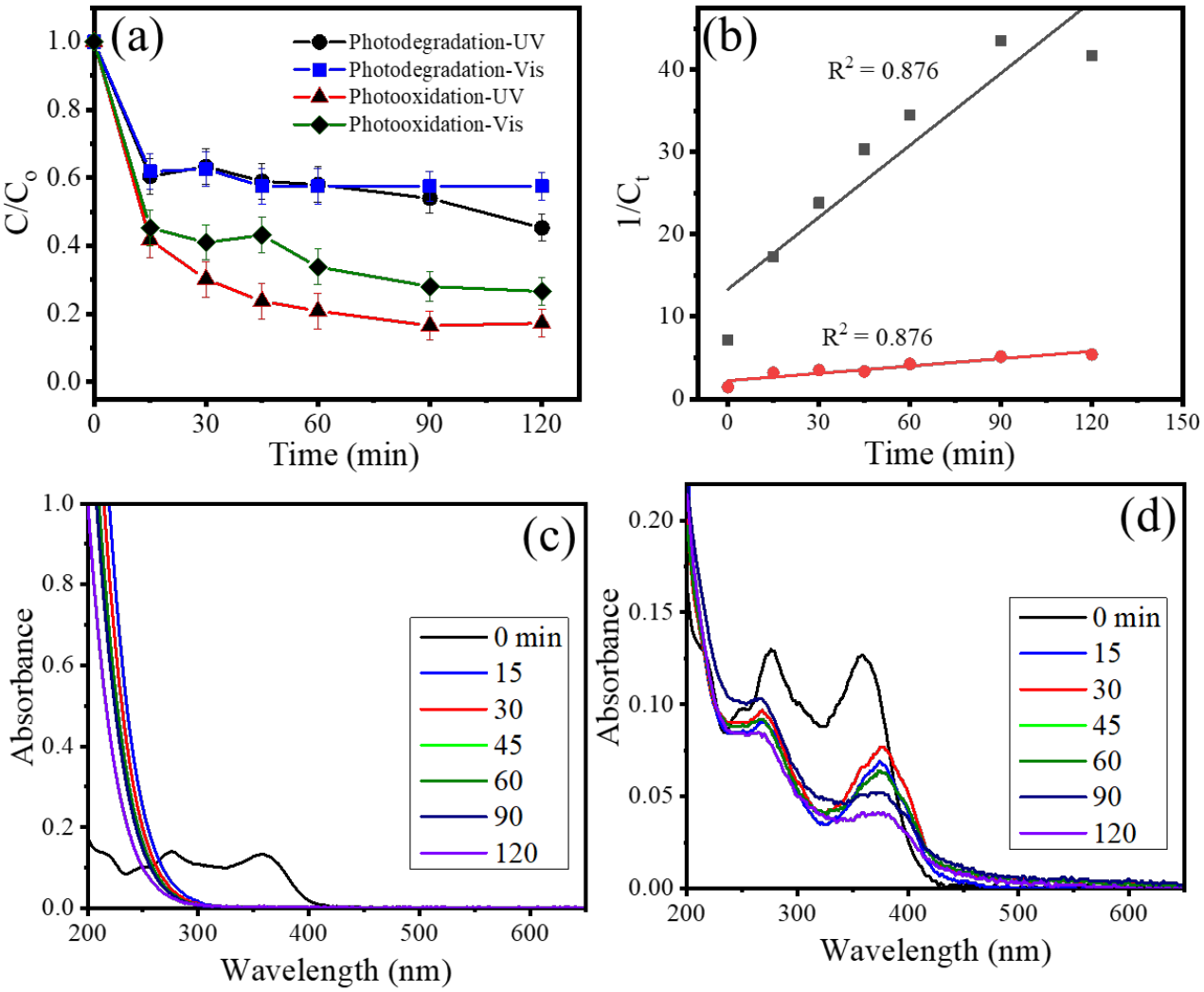

Figure 9. a. Kinetics Plot of TC Removal by Photodegradation and Photooxidation Using Ni(CT)/HA, b. Pseudo-Second Order Kinetic Plots of TC Using Ni(CT)/HA, (c-d) Spectral Change of Treated TC Solution by Photooxidation and Photodegradation, Respectively

Table 2. Kinetics Data of TC Removal By Photodegradation and Photooxidation Using Prepared Samples

Photocatalyst	Treatment	Initial Rate (mg/L.min)	k	DE
Ni(CT)/HA	Photooxidation-UV	0.263	1.22×10^{-2}	83.78
Ni(CT)/HA	Photooxidation-Vis	0.221	8.92×10^{-3}	73.24
Ni(CT)/HA	Photodegradation-UV	0.196	4.82×10^{-3}	54.67
Ni(CT)/HA	Photodegradation-Vis	0.103	4.09×10^{-3}	31.03
Ni/HA	Photodegradation-UV	0.046	$1.27x10^{-2}$	53.00
Ni/HA	Photodegradation-Vis	0.041	$2.03 \times 10{-}3$	43.09

cell equilibrium and produce reactive oxygen species (ROS) (Figure 11). The ROS could completely inhibit the function of protein, mitochondria for DNA damage and cell lysis. The condition also drives the function of ATP-driven enzyme to convert the energy of ATP hydrolysis to electro-chemical potential (Ivankovic et al., 2023; Nisar et al., 2019).

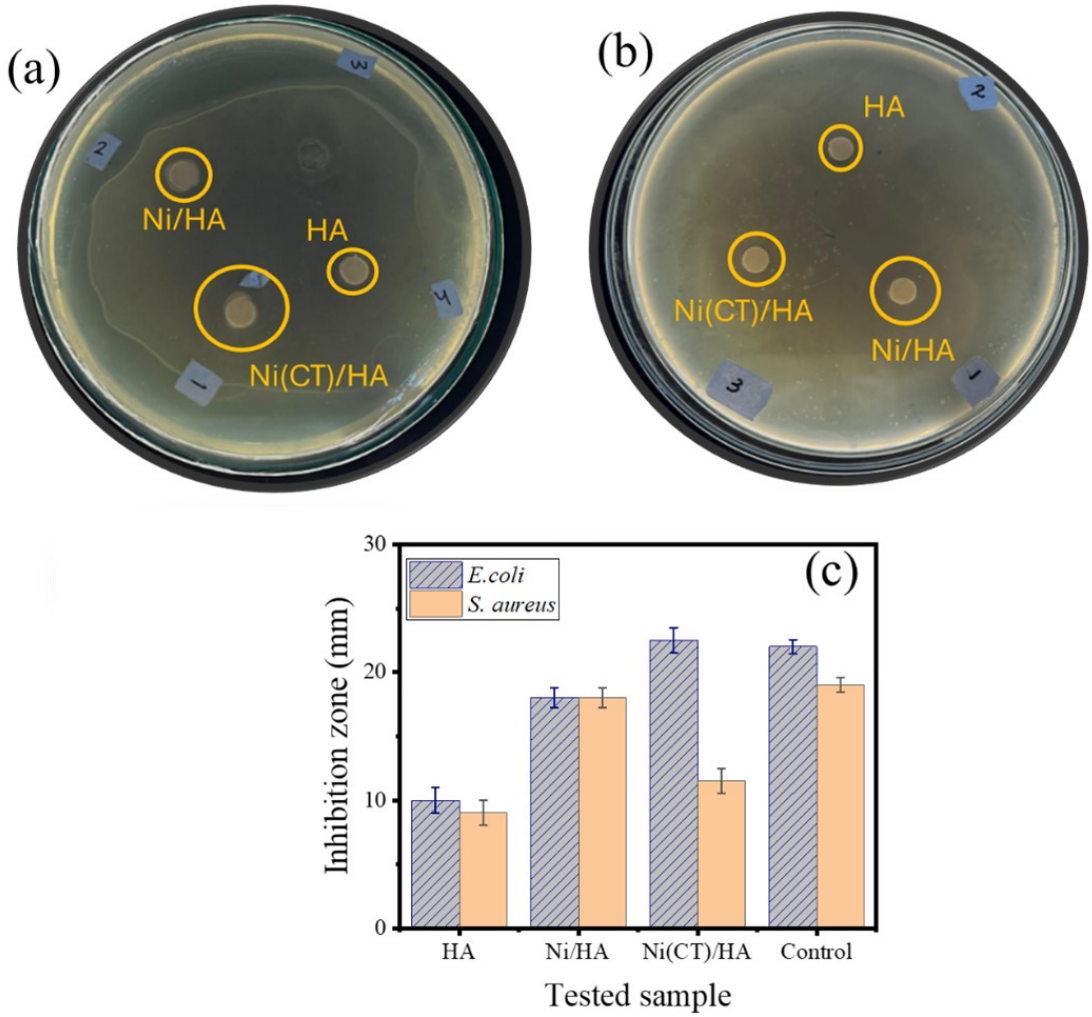

Figure 10. (a-b) Images from Antibacterial Assay Against *E. coli* and *S. aureus*, c. Recapitulated Inhibition Zone from Antibacterial Testing [Concentration of Sample = 40 mg/L]

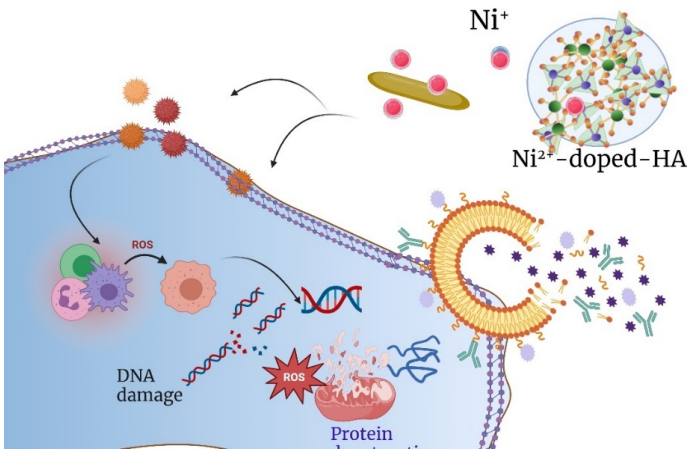

Figure 11. Antibacterial mechanism of Ni-doped HA

3.6 Ni/HA as Drug Delivery Agent

In order to investigate 5FU-functionalized HA and Ni/HA samples potential cell growth inhibition in CT26 cells, the effect of treatment on cells was examined with a MTT assay. As shown in Figure 12, the in vitro cell viability assay of CT26 cell lines incubated with HA, Ni/HA and Ni(CT)/HA for 48 h. It is seen that all tested samples represent a significant activity with a % decreased cell viability of higher than 80%. In more detail, the Ni(CT)/HA sample shows the highest decreased viability with following order: 5FU-Ni(CT)/HA> 5FU-Ni/HA> 5FU-HA. Moreover, the morphological changes that were captured under each condition demonstrate a major morphological difference was observed in cells treated with the samples, indicating a strong cellular response against the treatment. The highest influence of Ni(CT)/HA compared to Ni/HA revealed the significant influence of the synthesis method to the surface and drug release mechanism. In this case, HA and the Ni-doped forms act as drug delivery agents with theoretical structure as

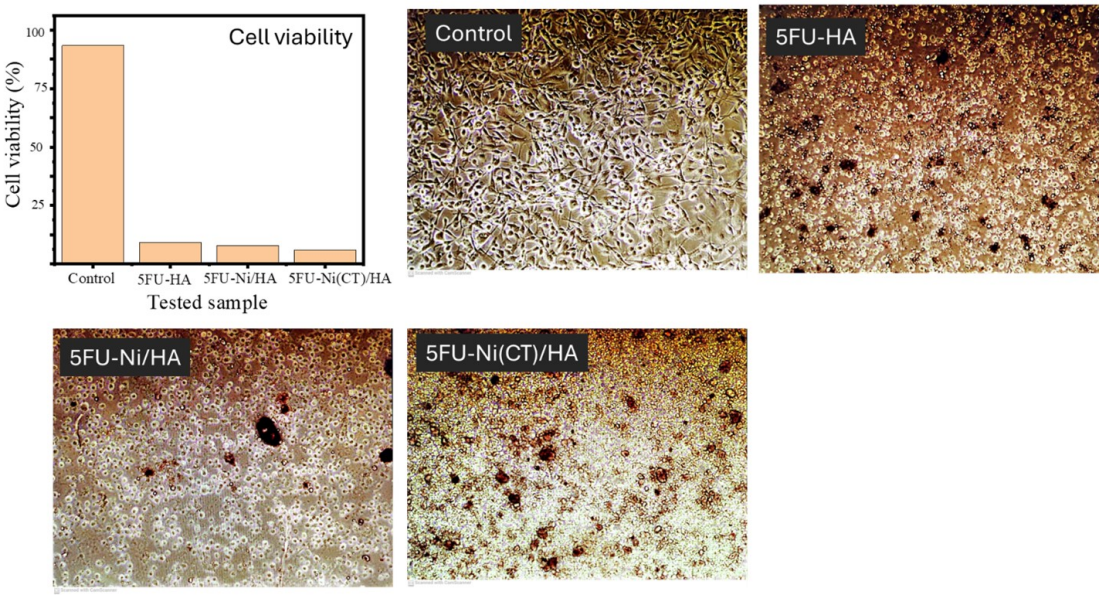

Figure 12. Cell Viability Test of Prepared Samples

Table 3. Comparison on the Antibacterial Activity of Metal-Doped HA

Material	Antibacterial Activity	Reference
Ag-doped HA	The sample demonstrated inhibition zone of 15 mm at concentration of 50 mg/L in testing against *S. aureus*	(Elbasuney et al., 2022)
Ag-doped HA	An inhibition zone of 15 mm was expressed by the sample at the concentration of 5 mg/mL against *E. coli*.	(Silva et al., 2007)
Ti-doped HA	An inhibition zone of 15 mm was expressed by the sample at the concentration of 50 mg/mL against *E. coli*.	(Fatimah et al., 2023)
Zn-doped HA	*S. aureus* bacteria growth was 50% inhibited by a concentration of 31.25 mg/mL of the sample, and with the same concentration, the *E. coli* was inhibited of around 20%.	(Predoi et al., 2019)
Ag/Zn-doped HA	The Ag/Zn- HA showed an excellent antibacterial activity as 99 ± 1% of *E. coli* obliterated at the concentration of 300 μg/mL.	(Sinulingga et al., 2021)
Sm/HA	Sm/HA exhibited viability and proliferation after 24 hours at around 100% relating to against *E. coli*.	(Ciobanu et al., 2015)
Ni-doped HA	At the concentration of 40 mg/mL, the material shows inhibition zone of 22.5 mm and 18 mm for *S. aureus* and *E. coli*, respectively.	This work

presented in Figure 12.

Referred to previous similar research on 5FU-functionalized nanomaterials, the mechanism of drug release is related to the slow leaching of 5FU into cell line (Mashaqbeh et al., 2024). Considering the presence of functional groups identified from FTIR analysis, the anticancer activity of the samples could be schematically described with Figure 13.

By comparing the cytotoxicity efficacy of HA expressed the decreasing cell viability of no more than 5% (Lamkhao et al., 2019), the immobilized Ni NPs and 5FU are the responsible agents to give cytotoxicity of the samples. The capability of Ni/HA for inhibiting cell growth is related to this effect on the production of reactive oxygen species. The presence of the samples leads to decreased dehydrogenase activity referring to the lower cellular ATP level, and furthermore causing damage to the mitochondrial respiratory chain, and other cellular components. Besides a disruption in cell membrane functions, NP gives cytotoxicity effect by growth inhibition and suppression via a unique intracellular mechanism. This condition is the mechanism occurring for the decreased cell viability against NPs. From the 5FU site which the structure is analogous to the nucleotide uracil, it has an ability to disrupt RNA

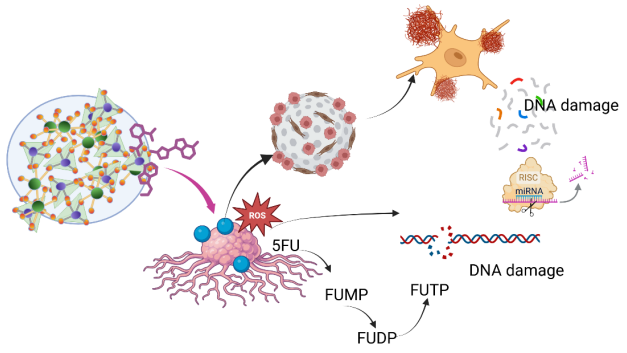

Figure 13. Schematic Representation of Anticancer Activity by Ni(CT)/HA

and the function by conversion into three primary metabolites: fluorouridine triphosphate (FUTP), fluorodeoxyuridine monophosphate (FUMP), and fluorodeoxyuridine diphosphate (FUDP). These metabolites will block the typical substrate deoxyuridine monophosphate that inhibits deoxythymidine monophosphate synthesis leading to deoxythymidine triphosphate imbalance.

Consequently, DNA damage will be caused by a deficiency of monophosphate (Olguin et al., 2023; Shakeri-Zadeh et al., 2014). By both anticancer mechanisms from the nanocomposite structure, the activity is higher compared to 5FU-immobilized magnetic nanoparticles reported from previous work which in the same concentration, the cell viability of 48h incubated cell is about 62.5% (Olguin et al., 2023), and rFU-immobilized graphene oxide (Afarideh et al., 2018). In similar way, the synergistic mechanism was also reported by the combination of 5FU with manganese nanoparticles (Olguin et al., 2023). The higher cytotoxicity of Ni(CT)/HA compared to Ni/HA is related to the different surface morphology which influence the binding interaction with 5FU. Some factors determining the cell proliferation inhibition by nanoparticles are size, homogeneous distribution, surface electronic state, and morphology (Altaee et al., 2020; Xu et al., 2022). The higher activity of Ni(CT)/HA compared to Ni/HA as drug-delivery agent is probably forced by the synergistic mechanism of the presence of β-TCP in the nanocomposite system (Diwan et al., 2024).

4. CONCLUSIONS

Conclusively, the synthesized nickel-doped hydroxyapatite using *Clitoria ternatea* extract exhibits the successful nickel doping into hydroxyapatite structure. The XRD and TEM analysis results showed the partial transformation of hydroxyapatite into β-TCP. The prepared nickel-doped hydroxyapatite exhibits the band gap energy of 2.95 eV and particle size ranging at 10-30 nm. The material showed capability to be photocatalyst for tetracycline removal by photodegradation and photooxidation mechanism. From the antibacterial activity examination, the prepared nickel-doped hydroxyapatite demonstrated a strongly potential activity against *E. coli* and *S. aureus*. The material also demonstrated capability to be drug delivery, especially for 5-fluorouracil, and the significant reduced cell viability of CT26 cell line. The results demonstrated a promising method of metal-doped hydroxyapatite for environmental and biomedical applications.

5. ACKNOWLEDGEMENT

Authors thank to Chemistry Department, Universitas Islam Indonesia for supporting this research through Hibah Penelitian Kerjasama Contract No: 003/Dir/DPPM/70/Pen.Kerjasama/I-V/2024 and collaborative research with Institute of Medical Science Technology, Universiti Kuala Lumpur, NANOCAT, University of Malaya, and Hanseo University.

REFERENCES

Abdel-Aal, E. A., D. El-Sayed, and H. M. Abdel-Ghafar (2024). Hydrothermal Synthesis of Hydroxyapatite Crystals With and Without Seed Crystals and Surfactant. *Discover Applied Sciences*, **6**(4); 143

Afarideh, B., M. Rajabibazl, M. Omidi, A. Bahramyaghmaee, Rahimpour, R. Khodabakhshi, and S. Sarvarian (2018). Anticancer Activity of Graphene Oxide/5-Fu on CT26 DSRED Adenocarcinoma Cell Line. *Oriental Journal of Chemistry*, **34**(4); 2002–2007

Al-darwesh, M. Y., S. S. Ibrahim, and M. A. Mohammed (2024). A Review on Plant Extract Mediated Green Synthesis of Zinc Oxide Nanoparticles and Their Biomedical Applications. *Results in Chemistry*, **7**; 101368

Alorku, K., M. Manoj, and A. Yuan (2020). A Plant-Mediated Synthesis of Nanostructured Hydroxyapatite for Biomedical Applications: A Review. *RSC Advances*, **10**(67); 40923–40939

Altaee, M. F., L. A. Yaaqoob, and Z. K. Kamona (2020). Evaluation of the Biological Activity of Nickel Oxide Nanoparticles as Antibacterial and Anticancer Agents. *Iraqi Journal of Science*, **61**(11); 2888–2896

Anastasiou, A. D., C. L. Thomson, S. A. Hussain, T. J. Edwards, S. Strafford, M. Malinowski, and A. Jha (2016). Sintering of Calcium Phosphates with a Femtosecond Pulsed Laser for Hard Tissue Engineering. *Materials and Design*, **101**; 346–354

Azizi, A. (2020). Green Synthesis of Fe_3O_4 Nanoparticles and Its Application in Preparation of Fe_3O_4/Cellulose Magnetic Nanocomposite: A Suitable Proposal for Drug Delivery Systems. *Journal of Inorganic and Organometallic Polymers and Materials*, **30**(9); 3552–3561

Balto, H., M. Amina, R. S. Bhat, H. M. Al-Yousef, S. H. Auda, and A. Elansary (2023). Green Synthesis of Nickel Nanoparticles Using *Salvadora persica* and Their Application in An-

timicrobial Activity Against Oral Microbes. *Microbiology Research*, **14**(4); 1879–1893

Berkün Olgun, O., B. Palas, S. Atalay, and G. Ersöz (2021). Photocatalytic Oxidation and Catalytic Wet Air Oxidation of Real Pharmaceutical Wastewater in the Presence of Fe and $LaFeO_3$ Doped Activated Carbon Catalysts. *Chemical Engineering Research and Design*, **171**; 421–432

Chen, Y., J. Yang, L. Zeng, and M. Zhu (2022). Recent Progress on the Removal of Antibiotic Pollutants Using Photocatalytic Oxidation Process. *Critical Reviews in Environmental Science and Technology*, **52**(8); 1401–1448

Ciobanu, C. S., S. L. Iconaru, C. L. Popa, M. Motelica-Heino, and D. Predoi (2015). Evaluation of Samarium Doped Hydroxyapatite, Ceramics for Medical Application: Antimicrobial Activity. *Journal of Nanomaterials*, **2015**(1); 849216

Diwan, H., S. Dan, and M. K. Sah (2024). Synergistic Effect of Waste-Derived β-Tricalcium Phosphate Microbeads Loaded in Hydroxyapatite-Keratin-Polyvinyl Alcohol Composite Matrix in Drug Release for Osteosarcoma Treatment. *Future Journal of Pharmaceutical Sciences*, **10**(1); 109

Elbasuney, S., G. S. El-Sayyad, S. M. Radwan, and M. A. Correa-Duarte (2022). Antimicrobial and Antibiofilm Activities of Silver Doped Hydroxyapatite: A Novel Bioceramic Material for Dental Filling. *Journal of Inorganic and Organometallic Polymers and Materials*, **32**(12); 4559–4575

Far, H., M. Hamici, N. Brihi, K. Haddadi, M. Boudissa, T. Chihi, and M. Fatmi (2022). High-Performance Photocatalytic Degradation of NiO Nanoparticles Embedded on α-Fe_2O_3 Nanoporous Layers Under Visible Light Irradiation. *Journal of Materials Research and Technology*, **19**; 1944–1960

Fatimah, I., P. W. Citradewi, G. Fadillah, I. Sahroni, G. Purwiandono, and R. A. Dong (2021a). Enhanced Performance of Magnetic Montmorillonite Nanocomposite as Adsorbent for Cu(II) by Hydrothermal Synthesis. *Journal of Environmental Chemical Engineering*, **9**(1); 104968

Fatimah, I., P. W. Citradewi, A. Yahya, B. H. Nugroho, H. Hidayat, G. Purwiandono, and S. Ibrahim (2021b). Biosynthesized Gold Nanoparticles-Doped Hydroxyapatite as Antibacterial and Antioxidant Nanocomposite. *Materials Research Express*, **8**(11); 0–10

Fatimah, I., H. Hidayat, P. W. Citradewi, M. Tamyiz, R. A. Doong, and S. Sagadevan (2023). Hydrothermally Synthesized Titanium/Hydroxyapatite as Photoactive and Antibacterial Biomaterial. *Heliyon*, **9**(3); e14434

Fatimah, I., H. Hidayat, B. H. Nugroho, and S. Husein (2020). Ultrasound-Assisted Biosynthesis of Silver and Gold Nanoparticles Using *Clitoria ternatea* Flower. *South African Journal of Chemical Engineering*, **34**; 97–106

Fatimah, I., H. Hidayat, G. Purwiandono, K. Khoirunisa, H. A. Zahra, R. Audita, and S. Sagadevan (2022). Green Synthesis of Antibacterial Nanocomposite of Silver Nanoparticle-Doped Hydroxyapatite Utilizing *Curcuma longa* Leaf Extract and Land Snail (*Achatina Fulica*) Shell Waste. *Journal of Functional Biomaterials*, **13**(2); 84

Fatimah, I., G. D. Ramanda, S. Sagadevan, Suratno, M. Tamyiz, and R. A. Doong (2024). One-Pot Synthesis of Nickel Nanoparticles-Embedded Biochar and Insight on Adsorption, Catalytic Oxidation and Photocatalytic Oxidation of Dye. *Case Studies in Chemical and Environmental Engineering*, **10**; 100767

Fihri, A., C. Len, R. S. Varma, and A. Solhy (2017). Hydroxyapatite: A Review of Syntheses, Structure and Applications in Heterogeneous Catalysis. *Coordination Chemistry Reviews*, **347**; 46–76

Haider, A. J., R. Al-Anbari, H. M. Sami, and M. J. Haider (2019). Photocatalytic Activity of Nickel Oxide. *Journal of Materials Research and Technology*, **8**(3); 2802–2808

Ilbeigi, G., A. Kariminik, and M. H. Moshafi (2019). The Antibacterial Activities of NiO Nanoparticles Against Some Gram-Positive and Gram-Negative Bacterial Strains. *International Journal of Basic Science in Medicine*, **4**(2); 69–74

In, Y., U. Amornkitbamrung, M. H. Hong, and H. Shin (2020). On the Crystallization of Hydroxyapatite Under Hydrothermal Conditions: Role of Sebacic Acid as an Additive. *ACS Omega*, **5**(42); 27204–27210

Ivankovic, T., H. Turk, J. Hrenovic, Z. Schauperl, M. Ivankovic, and A. Ressler (2023). Antibacterial Activity of Silver Doped Hydroxyapatite Toward Multidrug-Resistant Clinical Isolates of Acinetobacter baumannii. *Journal of Hazardous Materials*, **458**; 131867

Jeyaraj, E. J., Y. Y. Lim, and W. S. Choo (2021). Extraction Methods of Butterfly Pea (*Clitoria ternatea*) Flower and Biological Activities of Its Phytochemicals. *Journal of Food Science and Technology*, **58**(6); 2054–2067

Jiji, K. N. and P. Muralidharan (2021). Identification and Characterization of Phytoconstituents of Ethanolic Root Extract of *Clitoria ternatea* L. Utilizing HR-LCMS Analysis. *Plant Science Today*, **8**(3); 535–540

Kanasan, N., S. Adzila, H. A. Rahman, N. Bano, G. Panerselvan, and N. A. Hidayati (2018). FTIR and XRD Evaluation of Magnesium Doped Hydroxyapatite/Sodium Alginate Powder by Precipitation Method. *Key Engineering Materials*, **791**; 45–49

Kanchana, P. and C. Sekar (2012). Effect of Magnesium on the Mechanical and Bioactive Properties of Biphasic Calcium Phosphate. *Journal of Minerals and Materials Characterization and Engineering*, **11**(10); 982–988

Khwannimit, D., R. Maungchang, and P. Rattanakit (2020). Green Synthesis of Silver Nanoparticles Using *Clitoria ternatea* Flower: An Efficient Catalyst for Removal of Methyl Orange. *International Journal of Environmental Analytical Chemistry*, **102**(17); 5247–5263

Kurinjinathan, P., J. Thanigai Arul, E. Ramana Ramya, M. H. H, A. Hegazy, Umar, and N. Ahmad (2020). Effect of Nickel Doping on the Properties of Hydroxyapatite Nanoparticles. *Journal of Nanoscience and Nanotechnology*, **20**(4); 2482–2487

Lamkhao, S., M. Phaya, C. Jansakun, N. Chandet, K. Thongkorn, G. Rujijanagul, and C. Randorn (2019). Synthesis of Hydroxyapatite with Antibacterial Properties Using

a Microwave-Assisted Combustion Method. *Scientific Reports*, **9**(1); 1–9

Liang, W., Y. Niu, S. Ge, S. Song, J. Su, and Z. Luo (2012). Effects of Hydrothermal Treatment on the Properties of Nanoapatite Crystals. *International Journal of Nanomedicine*, **7**; 5151–5158

Mardziah, C. M., N. R. N. Masdek, N. M. Mubarak, and S. Ramesh (2023). Characteristics of Zinc-Doped Hydroxyapatite Prepared Using Biogenic and Synthetic Calcium Precursor. *Proceeding of 5th International Conference on Advances in Manufacturing and Materials Engineering*; 175–181

Mashaqbeh, H., R. Obaidat, M. M. Alsmadi, S. Bardaweel, and N. Hailat (2024). Characterization and Optimization of Colon Specific Nanosponges Immobilized Polymeric Microbeads Formulation for the Combined Delivery of 5-Fluorouracil and Curcumin. *Journal of Drug Delivery Science and Technology*, **99**; 105968

Mayer, I., F. J. G. Cuisinier, S. Gdalya, and I. Popov (2008). TEM Study of the Morphology of Mn^{2+}-Doped Calcium Hydroxyapatite and β-Tricalcium Phosphate. *Journal of Inorganic Biochemistry*, **102**(2); 311–317

Mohammad, M. K., S. H. Ahmed, and R. A. J. Alameri (2021). Green Medicine: A Novel Preparation Method for Green Synthesizing of Iron Nanoparticles Derived from *Beta vulgaris* Extract. *Archives of Razi Institute*, **76**(5); 1109–1114

Mohammed, E., B. Tbib, and K. El-Hami (2018). High Photocatalytic Activity of Hydroxyapatite Bio-Degradable Semiconductor for Solar Panels and Environment Protection. *ISTE OpenScience*; 1–8

Mondal, S., S. Park, J. Choi, T. T. H. Vu, V. H. M. Doan, T. T. Vo, and J. Oh (2023). Hydroxyapatite: A Journey from Biomaterials to Advanced Functional Materials. *Advances in Colloid and Interface Science*, **321**; 103013

Naveenkumar, R. and G. Baskar (2021). Process Optimization, Green Chemistry Balance and Technoeconomic Analysis of Biodiesel Production from Castor Oil Using Heterogeneous Nanocatalyst. *Bioresource Technology*, **320**; 124347

Nicácio, T. C. N., M. A. M. Castro, M. C. N. Melo, T. A. Silva, M. D. Teodoro, M. R. D. Bomio, and F. V. Motta (2024). Zn and Ni Doped Hydroxyapatite: Study of the Influence of the Type of Energy Source on the Photocatalytic Activity and Antimicrobial Properties. *Ceramics International*, **50**(15); 27540–27552

Nisar, P., N. Ali, L. Rahman, M. Ali, and Z. K. Shinwari (2019). Antimicrobial Activities of Biologically Synthesized Metal Nanoparticles: An Insight into the Mechanism of Action. *Journal of Biological Inorganic Chemistry*, **24**(7); 929–941

Olguin, J. E., M. G. Mendoza-Rodriguez, C. A. Sanchez-Barrera, and L. I. Terrazas (2023). Is the Combination of Immunotherapy with Conventional Chemotherapy the Key to Increase the Efficacy of Colorectal Cancer Treatment? *World Journal of Gastrointestinal Oncology*, **15**(2); 251–267

Poh Yan, L., S. C. B. Gopinath, S. Subramaniam, Y. Chen, P. Velusamy, S. V. Chinni, and V. R. Lebaka (2022). Greener Synthesis of Nanostructured Iron Oxide for Medical and Sustainable Agro-Environmental Benefits. *Frontiers in Chemistry*, **10**; 1–15

Prabhu, S., T. D. Thangadurai, P. V. Bharathy, and P. Kalugasalam (2022). Investigation on the Photocatalytic and Antibacterial Activities of Green Synthesized Cupric Oxide Nanoparticles Using *Clitoria ternatea*. *Iranian Journal of Catalysis*, **12**(1); 394–400

Predoi, D., S. L. Iconaru, M. V. Predoi, M. Motelica-Heino, R. Guegan, and N. Buton (2019). Evaluation of Antibacterial Activity of Zinc-Doped Hydroxyapatite Colloids and Dispersion Stability Using Ultrasounds. *Nanomaterials*, **9**(4); 515

Prekajski, M., B. Jokíc, A. Kalijadis, J. Maletaškíc, N. Stankovíc, J. Lukovíc, and B. Matovíc (2016). Synthesis of Silver Doped Hydroxyapatite Nanospheres Using Ouzo Effect. *Processing and Application of Ceramics*, **10**(3); 169–174

Robles-Águila, M. J., J. A. Reyes-Avendano, and M. E. Mendoza (2017). Structural Analysis of Metal-Doped (Mn, Fe, Co, Ni, Cu, Zn) Calcium Hydroxyapatite Synthetized by a Sol-Gel Microwave-Assisted Method. *Ceramics International*, **43**(15); 12705–12709

Scharnweber, T., C. Santos, R. P. Franke, M. M. Almeida, and M. E. V. Costa (2008). Influence of Spray-Dried Hydroxyapatite-5-Fluorouracil Granules on Cell Lines Derived From Tissues of Mesenchymal Origin. *Molecules*, **13**(11); 2729–2739

Shaheen, J., Y. H. Fseha, and B. Sizirici (2022). Performance, Life Cycle Assessment, and Economic Comparison Between Date Palm Waste Biochar and Activated Carbon Derived From Woody Biomass. *Heliyon*, **8**(12); e12388

Shakeri-Zadeh, A., M. B. Shiran, S. Khoee, A. M. Sharifi, H. Ghaznavi, and S. Khoei (2014). A New Magnetic Nanocapsule Containing 5-Fluorouracil: In Vivo Drug Release, Anti-Tumor, and Pro-Apoptotic Effects on CT26 Cells Allograft Model. *Journal of Biomaterials Applications*, **29**(4); 548–556

Silva, C. C., M. P. F. Graça, M. A. Valente, and A. S. B. Sombra (2007). Crystallite Size Study of Nanocrystalline Hydroxyapatite and Ceramic System With Titanium Oxide Obtained by Dry Ball Milling. *Journal of Materials Science*, **42**(11); 3851–3855

Sinulingga, K., M. Sirait, N. Siregar, and M. E. Doloksaribu (2021). Investigation of Antibacterial Activity and Cell Viability of Ag/Mg and Ag/Zn Co-Doped Hydroxyapatite Derived From Natural Limestone. *ACS Omega*, **6**(49); 34185–34191

Sundrarajan, M., S. Jegatheeswaran, S. Selvam, N. Sanjeevi, and M. Balaji (2015). The Ionic Liquid Assisted Green Synthesis of Hydroxyapatite Nanoplates by *Moringa oleifera* Flower Extract: A Biomimetic Approach. *Materials and Design*, **88**; 1183–1190

Unal, I., B. Aydogdu, and M. Aytar (2024). Plant Extract-Based Biosynthesis of Silver Nanoparticle and Silver–Zinc Nanocomposites-Doped Hydroxyapatite and Its Antimicrobial Activity. *Advances in Applied Ceramics: Structural, Func-*

tional and Bioceramics, **123**(1–3)

Varadavenkatesan, T., R. Vinayagam, S. Pai, B. Kathirvel, A. Pugazhendhi, and R. Selvaraj (2021). Synthesis, Biological and Environmental Applications of Hydroxyapatite and Its Composites With Organic and Inorganic Coatings. *Progress in Organic Coatings*, **151**; 106056

Wang, Y., X. Yang, Z. Gu, H. Qin, L. Li, J. Liu, and X. Yu (2016). In Vitro Study on the Degradation of Lithium-Doped Hydroxyapatite for Bone Tissue Engineering Scaffold. *Materials Science and Engineering C*, **66**; 185–192

Xu, J. J., W. C. Zhang, Y. W. Guo, X. Y. Chen, and Y. N. Zhang (2022). Metal Nanoparticles as a Promising Technology in Targeted Cancer Treatment. *Drug Delivery*, **29**(1); 664–678

Yadav, M. K., R. H. Shukla, and K. G. P. C (2023). A Comprehensive Review on Development of Waste Derived Hydroxyapatite (HAp) for Tissue Engineering Application. *Materials Today: Proceedings*, **(in Press)**

Yeshchenko, O. A., V. V. Kozachenko, and A. V. Tomchuk (2018). Surface Plasmon Resonance in "Monolayer of Ni Nanoparticles/Dielectric Spacer/Au (Ni) Film" Nanostructure: Tuning by Variation of Spacer Thickness. *Ukrainian Journal of Physics*, **63**(5); 386–395

Yilmaz, G. E., I. Göktürk, M. Ovezova, F. Yilmaz, S. Kilic, and A. Denizli (2023). Antimicrobial Nanomaterials: A Review. *Hygiene*, **3**(3); 269–290

Yoga Darmawan, M., N. Imani Istiqomah, N. Adrianto, R. Marsel Tumbelaka, A. Dwi Nugraheni, and E. Suharyadi (2023). Green Synthesis of Fe_3O_4/Ag Composite Nanoparticles Using *Moringa oleifera*: Exploring Microstructure, Optical, and Magnetic Properties for Magnetic Hyperthermia Applications. *Results in Chemistry*, **6**; 100999

Yuan, Q., J. Wu, C. Qin, A. Xu, Z. Zhang, Y. Lin, and P. Zhang (2017). One-Pot Synthesis and Characterization of Zn-Doped Hydroxyapatite Nanocomposites. *Materials Chemistry and Physics*, **199**; 122–130

